Equation-of-Motion Coupled-Cluster Theory to Model L-edge X-Ray Absorption and Photoelectron Spectra

Marta L. Vidal,[*,†] Pavel Pokhilko,[‡,¶] Anna I. Krylov,[‡] and Sonia Coriani[*,†]

†*DTU Chemistry - Department of Chemistry, Technical University of Denmark, Kemitorvet Bldg 207, DK-2800, Kongens Lyngby, Denmark*

‡*Department of Chemistry, University of Southern California, Los Angeles, California 90089-0482*

¶*Current address: Department of Chemistry, University of Michigan, Ann Arbor, MI 48109, USA*

E-mail: malop@kemi.dtu.dk; soco@kemi.dtu.dk

Abstract

We present an extension of the equation-of-motion coupled-cluster singles and doubles (EOM-CCSD) theory for computing x-ray L-edge spectra, both in the absorption (XAS) and photoelectron (XPS) regimes. The approach is based on the perturbative evaluation of spin-orbit couplings using the Breit-Pauli Hamiltonian and non-relativistic wave-functions described by the fc-CVS-EOM-CCSD ansatz (EOM-CCSD within the frozen-core core-valence separated (fc-CVS) scheme). The formalism is based on spinless one-particle density matrices. The approach is illustrated by modeling XAS and XPS of several model systems ranging from argon atoms to small molecules containing sulfur and silicon.

Graphical TOC Entry

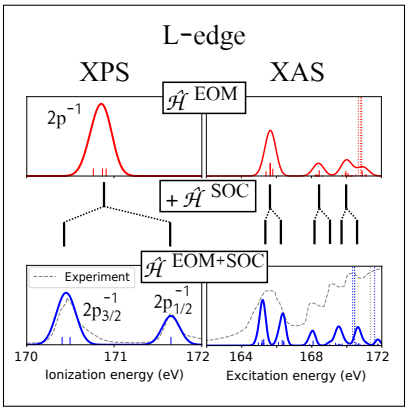

Keywords

Inner-shell 2p spectra, spin-orbit coupling, coupled-cluster theory, equation-of-motion, core-valence separation, Breit-Pauli Hamiltonian

Spectroscopic techniques exploiting x-ray radiation have a long history. Two of the most popular ones, x-ray absorption (XAS) and x-ray photoemission (XPS, also known as x-ray photoelectron or electron spectroscopy for chemical analysis, ESCA), enable investigation of the local electronic structure in molecules and materials. The 21st century generation of light sources, ranging from synchrotron and x-ray free-electron lasers to table-top x-ray instruments based on high harmonic generation, facilitate exciting new experiments, which were merely hypothetical just a few years back. These advances have triggered an explosion of interest of the molecular and material sciences community in the x-ray based techniques.[1–3] The advances in the experimental tools are accompanied by the boost of activity in the development of theoretical methods for simulating and interpreting experimental spectra.[4]

Conceptually, x-ray spectroscopy is similar to UV-Vis spectroscopy, the main difference being the energy scale and, consequently, the type of electronic transitions that are probed. UV-Vis radiation induces transitions involving the outer-shell valence electrons, whereas x-ray radiation induces transitions involving inner-shell core electrons. Despite this similarity, the theoretical methods developed for valence spectroscopy are not directly applicable to model core-level spectroscopies.[4] Similarly to their valence counterparts, core-level states often have open-shell character, but they also exhibit strong orbital relaxation. Thus, their description requires sufficiently flexible basis sets[5,6] and many-body ansatze that are capable of tackling static and dynamical correlation as well as orbital relaxation.

The equation-of-motion (EOM) coupled-cluster (CC) framework[7–12] is a versatile platform for treating excited and ionized states with open-shell character. Even at the lowest level of correlation treatment, when only single and double excitations are included in the ansatz, the method has the ability to tackle both dynamic correlation and orbital relaxation. Originally, EOM-CC was developed to study valence states; thus, typical implementations seek the solutions corresponding to the lowest-lying states, which is obviously not suitable for high-energy core-level states. Another complication arises from the fact that the core-level states are embedded in a continuum of valence excited and ionized states, which leads

to poor convergence and erratic results.[13,14] An effective solution to these two problems is given by the core-valence separation (CVS) scheme,[15] which decouples the valence and core sectors of the Fock space, on the basis of the large energy gap between the core and valence orbitals. This idea, which provides a simple recipe for extending methods targeting valence states into the core-level domain, has been implemented within various electronic structure methods,[16–21] including the EOM-CC family.[22–24] The resulting methods have been successfully applied to model a variety of x-ray spectroscopic experiments such as absorption (XAS),[22,23,25,26] photoelectron (XPS),[24,27,28] x-ray emission (XES) and resonant inelastic scattering (RIXS).[14,29–31] At the CC level, the applications have been so far limited to the study of $1s$ electrons of light elements (that is, the K-edge), due to yet another obstacle towards the quantitative simulation of x-ray spectra—the need to include relativistic effects.

Relativistic effects, which become more pronounced at higher energies, can be classified into two categories: scalar and spin-orbit.[32] The first type is not critically important in the context of K-edge spectroscopy, because it results in a constant energy shift of the entire spectrum.[5,27,33] Because K-edge states are mostly affected by scalar relativistic effects, non-relativistic calculations yield qualitatively correct K-edge spectra. The second type, spin-orbit coupling (SOC), which arises from the coupling between the magnetic moment associated with the spin of the electron and the magnetic field created by the relative motion of charged particles (electrons and nuclei),[34] has a greater impact on the spectra at lower edges. SOC mixes states with different multiplicity, which do not interact in a non-relativistic picture. It also causes energy splittings of orbitals with nonzero orbital angular momentum ($l > 0$). Fig. 1 shows the SO splitting of the atomic $2p$ orbitals, illustrating that SOC considerably affects the L-edge spectra, by splitting them into two edges: an L_2 (or L_{II}) and an L_3 (or L_{III}) edge.

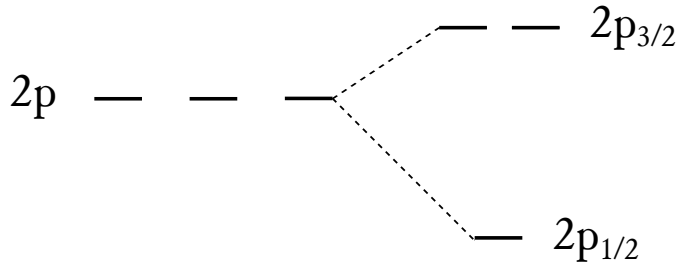

Figure 1: Splitting of the $2p$ orbitals due to spin-orbit coupling.

These effects can be fully accounted for within a fully relativistic treatment with a 4-component Hamiltonian,[35–37] but such treatments come with a substantial increase of the computational cost. Various flavors of two-component methods, such as the zeroth-order regular approximation (ZORA)[38–41] and its infinite-order variant (IORA),[42] the Douglas-Kroll-Hess method[43–45] or the exact 2-component (X2C) method,[46,47] are less demanding; however, these calculations still increase the computational cost by an order of magnitude relative to the non-relativistic calculation.[48] Furthermore, a variational treatment of the spin-orbit operator may lead to an imbalanced description of electronic states with different spin projections, resulting in the violation of Kramers theorem and momentum contamination.[49]

Fortunately, in molecules composed of atoms from the first few rows of the periodic table, perturbative treatment of SOC, which entails calculation of the matrix elements of the Breit-Pauli Hamiltonian using non-relativistic wave-functions, is sufficiently accurate while being computationally affordable.[50] This strategy, which has been successfully used within EOM-CC framework,[48,51–55] has not yet been extended to core-level spectroscopy, which is the focus of this communication. Building upon our previous work,[23,24,54–56] we implemented calculations of SOC within the frozen core (fc) CVS-EOM-CCSD method, thus extending the EOM-CC framework to modeling x-ray absorption and photoelectron spectroscopy at the L and higher (energetically lower) edges.

In this approach, the final states and their properties (energies and transition strengths) are obtained in a two-step procedure. In the first step, the non-relativistic states are com-

puted using the fc-CVS-EOM-CCSD ansatz:

$$|\Psi_{\text{fc-CVS-EOM}}\rangle = \hat{\mathcal{R}}_{\text{CVS}} e^{\hat{\mathcal{T}}_{\text{fc}}} |\Phi_0\rangle; \qquad \hat{\mathcal{T}}_{\text{fc}} = \sum_{\mu_v} t_{\mu_v} \hat{\tau}_{\mu_v}; \quad \hat{\mathcal{R}}_{\text{CVS}} = \sum_{\mu_c} t_{\mu_c} \hat{\tau}_{\mu_c}, \tag{1}$$

where $\hat{\mathcal{T}}$ and $\hat{\mathcal{R}}$ are the cluster and the EOM excitation operators, and the sub-indices v and c refer to valence and core orbital spaces, respectively. The exact form of the $\hat{\mathcal{R}}$ operator depends on the target-state manifold, giving rise to different flavors of EOM-CC methods. Here, we use EOM-IP (EOM for ionization potentials) to compute ionized states, EOM-EE (EOM for excitation energies) to compute singlet excited states, and EOM-SF (EOM spin-flip) to compute triplet excited states (with spin projection $m_s = -1$). For closed-shell systems, such as studied here, these calculations employ closed-shell reference states. In the second step, SOCs are calculated as the matrix elements of the spin-orbit part of the Breit-Pauli Hamiltonian, given in atomic units by:[57]

$$\hat{\mathcal{H}}^{\text{SO}} = \frac{1}{2c^2} \left(\sum_i \mathbf{h}^{\text{SO}}(i) \cdot \mathbf{s}(i) - \sum_{i \neq j} \mathbf{h}^{\text{SO}}(i,j) \cdot (\mathbf{s}(i) + 2\mathbf{s}(j)) \right), \tag{2}$$

where $\mathbf{h}^{\text{SO}}(i)$ and $\mathbf{h}^{\text{SO}}(i,j)$ are the one- and two-electron operators[58]

$$\mathbf{h}^{\text{SO}}(i) = \sum_K \frac{Z_K (\mathbf{r}_i - \mathbf{R}_K) \times \mathbf{p}_i}{|\mathbf{r}_i - \mathbf{R}_K|^3} = \sum_K \frac{Z_K}{r_{iK}^3} (\mathbf{r}_{iK} \times \mathbf{p}_i) = \sum_K \frac{Z_K}{r_{iK}^3} \mathbf{l}_{iK}, \tag{3}$$

$$\mathbf{h}^{\text{SO}}(i,j) = \frac{(\mathbf{r}_i - \mathbf{r}_j) \times \mathbf{p}_i}{|\mathbf{r}_i - \mathbf{r}_j|^3} = \frac{1}{r_{ij}^3} \mathbf{r}_{ij} \times \mathbf{p}_i = \frac{1}{r_{ij}^3} \mathbf{l}_{ij}, \tag{4}$$

$\mathbf{r}_i$, $\mathbf{p}_i$ and $\mathbf{l}_i$ are the coordinates and the (linear and angular) momenta, respectively, of electron i, and $\mathbf{R}_K$ and Z_K are the coordinates and nuclear charge of nucleus K. In second quantization, Eq. (2) assumes the following form:[54]

$$\hat{\mathcal{H}}^{\text{SO}} = \frac{1}{2c^2} \left(\sum_{pq} I_{pq} \hat{a}_p^\dagger \hat{a}_q + \frac{1}{2} \sum_{pqrs} J_{pqrs} \hat{a}_p^\dagger \hat{a}_q^\dagger \hat{a}_s \hat{a}_r \right), \tag{5}$$

where I and J refer to the one- and two-electron spin-orbit integrals:

$$I_{pq} = \langle \phi_p(1) | \mathbf{h}^{\mathrm{SO}}(1) \cdot \mathbf{s}(1) | \phi_q(1) \rangle, \tag{6}$$

$$J_{pqrs} = -\langle \phi_p(1)\phi_q(2) | \mathbf{h}^{\mathrm{SO}}(1,2) \cdot (\mathbf{s}(1) + 2\mathbf{s}(2)) | \phi_r(1)\phi_s(2) \rangle. \tag{7}$$

Matrix elements of this operator can be computed by contracting the spin-orbit integrals with the corresponding one- and two-electron transition density matrices (TDM):

$$\langle \Psi(s, m_s) | \hat{\mathcal{H}}^{\mathrm{SO}} | \Psi'(s', m'_s) \rangle = \sum_{pq} I_{pq} \gamma_{pq} + \frac{1}{2} \sum_{pqrs} J_{pqrs} \Gamma_{pqrs} \tag{8}$$

with

$$\gamma_{pq} = \langle \Psi(s, m_s) | \hat{a}_p^\dagger \hat{a}_q | \Psi'(s', m'_s) \rangle, \tag{9}$$

$$\Gamma_{pqrs} = \langle \Psi(s, m_s) | \hat{a}_p^\dagger \hat{a}_q^\dagger \hat{a}_s \hat{a}_r | \Psi'(s', m'_s) \rangle. \tag{10}$$

The calculation of the SOCs, as defined by Eq. (2), entails computationally demanding two-electron part of $\hat{\mathcal{H}}^{\mathrm{SO}}$. Fortunately, the two-electron contributions can be effectively evaluated in a mean-field manner. Within this approximation, called the spin-orbit mean-field (SOMF),[59] the calculation of SOC requires only the one-electron TDM

$$\langle \Psi(s, m_s) | \hat{\mathcal{H}}^{\mathrm{SOMF}} | \Psi'(s', m'_s) \rangle = \sum_{pq} H_{pq}^{\mathrm{SOMF}} \gamma_{pq}, \tag{11}$$

with the following effective one-electron operator $\hat{\mathcal{H}}^{\mathrm{SOMF}}$:[51,52,54]

$$H_{pq}^{\mathrm{SOMF}} = I_{pq} + \frac{1}{2} \sum_{rs} \rho_{rs} \left(J_{prqs} - J_{prsq} - J_{rpqs} \right) \tag{12}$$

where ρ is the state density matrix of the reference determinant. The SOMF approximation simply entails neglecting the non-separable part of two-electron transition density matrix.[54] By converting these equations into the atomic orbital basis, one can evaluate the SOMF

integrals using efficient algorithms, such as those used for the Fock matrix builds.

To obtain the SO-split states, we then construct the SOMF Hamiltonian matrix in the basis of zeroth-order states and diagonalize it. The diagonal of the SOMF matrix can be chosen as the zeroth-order energy and the off-diagonal elements between two different states $\Psi(s, m_s)$ and $\Psi'(s', m'_s)$ are $\langle\Psi(s, m_s)|\hat{\mathcal{H}}^{\mathrm{SOMF}}|\Psi'(s', m'_s)\rangle$, which are computed as described in Ref. 55. The states entering these expressions are the ionized states ($s = 1, m_s = \pm 1/2$) when we calculate ionization energies, and the singlet ($s = 0, m_s = 0$) and triplet ($s = 1, m_s = -1, 0, +1$) excited states when we calculate excitation energies. The diagonalization of the SOMF Hamiltonian matrix yields the target SO-coupled states, whose eigenvalues are the energies of the SO-split states. To compute oscillator strengths for the transitions involving the SO-split states, as needed for the simulation of L-edge NEXAFS, we first construct the non-Hermitian electric dipole matrices between the ground-state Ψ_0 and the zeroth-order states $\Psi(s, m_s)$:

$$\boldsymbol{\mu}_\alpha^{f\leftarrow 0} = \langle\Psi^f(s, m_s)|\hat{\mu}_\alpha|\Psi_0\rangle; \qquad \boldsymbol{\mu}_\alpha^{0\leftarrow f} = \langle\Psi_0|\hat{\mu}_\alpha|\Psi^f(s, m_s)\rangle, \tag{13}$$

where α denotes the Cartesian components x, y, and z. These transition matrices are then transformed into the new basis of the SO-split states, by applying the transformation obtained from the diagonalization of $\mathbf{H}^{\mathrm{SOMF}}$:

$$\tilde{\boldsymbol{\mu}}_\alpha^2 = \mathbf{U}^\dagger \boldsymbol{\mu}_\alpha^{f\leftarrow 0} \boldsymbol{\mu}_\alpha^{0\leftarrow f} \mathbf{U}, \tag{14}$$

where the matrix $\mathbf{U}$ contains the eigenvectors of $\mathbf{H}^{\mathrm{SOMF}}$. (Note that, although geometric averaging of non-Hermitian estimates from Eq. (14) does not necessarily lead to a real positive number, the magnitude of the (very few) non-positive values for the systems considered here was negligible.) Finally, the oscillator strengths for the transitions between the ground state

and the target SO state $\tilde{f}$ are computed as:

$$f(\tilde{f} \leftarrow 0) = \frac{2}{3}\omega_{\tilde{f}} \sum_{\alpha=x,y,z} \tilde{\boldsymbol{\mu}}_{\alpha}^{2}. \tag{15}$$

In a similar fashion, the XPS intensities can be estimated from the squared norm of the Dyson orbitals. The latter are defined as overlap of the initial N-particle wavefunction and the final $(N-1)$-particle wavefunction of the ion. We indicate the initial wavefunction as Ψ_0 and the final (SO-split) one as $\Psi_{\tilde{f}}$. To highlight that in CC theory the left and right Dyson orbitals differ,[24,60–62] an additional index L or R is attached to the wavefunction/orbital

$$\phi_{\tilde{f}}^{d,R} = \langle \Psi_0^L | \hat{a}_p^\dagger | \Psi_{\tilde{f}}^R \rangle \; ; \qquad \phi_{\tilde{f}}^{d,L} = \langle \Psi_{\tilde{f}}^L | \hat{a}_p | \Psi_0^R \rangle \tag{16}$$

The target SO-split ionic state $\Psi_{\tilde{f}}$ is the linear combination of the NR ionic states Ψ_j

$$\Psi_{\tilde{f}}^R = \sum_j \Psi_j^R U_{j\tilde{f}} \; ; \qquad \Psi_{\tilde{f}}^L = \sum_j U_{\tilde{f}j}^* \Psi_j^L \tag{17}$$

so the left and right Dyson orbitals for the SO-split target state $\Psi_{\tilde{f}}$ become

$$\phi_{\tilde{f}}^{d,R} = \sum_j \langle \Psi_0^L | \hat{a}_p^\dagger | \Psi_j^R \rangle U_{j\tilde{f}} = \sum_p \left(\sum_j \gamma_p^{R,j} U_{j\tilde{f}} \right) \phi_p = \sum_p \tilde{\gamma}_p^{R,\tilde{f}} \phi_p \tag{18}$$

$$\phi_{\tilde{f}}^{d,L} = \sum_j U_{\tilde{f}j}^* \langle \Psi_j^L | \hat{a}_p | \Psi_0^R \rangle = \sum_p \left(\sum_j \gamma_p^{L,j} U_{\tilde{f}j}^* \right) \phi_p = \sum_p \tilde{\gamma}_p^{L,\tilde{f}} \phi_p \tag{19}$$

where we introduced the amplitudes of the EOM-CCSD Dyson orbitals corresponding to the transitions between the original non-relativistic EOM states[24,60]

$$\gamma_p^{R,j} = \langle \Psi_0^L | \hat{a}_p^\dagger | \Psi_j^R \rangle; \qquad \gamma_p^{L,j} = \langle \Psi_j^L | \hat{a}_p | \Psi_0^R \rangle. \tag{20}$$

Fig. 2 shows zero-order and SO-mixed Dyson orbitals for H_2S, illustrating the effect of SOC on the ionized states. SO interaction mixes non-relativistic electronic states, changing orbital

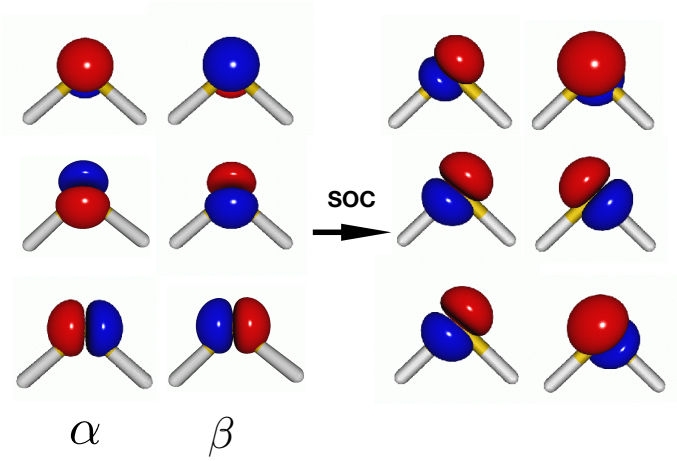

Figure 2: Left: Dyson orbitals for non-relativistic EOM-IP states. Right: Dyson orbitals of the SO-mixed states, obtained as linear combination of the regular atomic orbitals (AOs) with the Euclidean (left $\times$ right) norms of the complex Dyson orbital coefficients back-transformed to the AO basis.

shapes, i.e, $2p_{1/2}$ and $2p_{3/2}$ orbitals are rotated relative to the original p_x, p_y, and p_z, and also scrambling spin and space degrees of freedom. The SO-mixed orbitals also transform by different symmetry group (double point group). These SO-mixed Dyson orbitals illustrate the effect of the SOC on the ionized states, in the same fashion as the analysis of the SO-mixed transition density matrices from Ref. 63 illustrate the effect of SOC on the excited states. We note that this analysis is based on the SO-mixed adiabatic states, in contrast to the SOC NTO analysis presented in Ref. 56 formulated in terms of the non-relativistic (diabatic) states. The mixing also affects transition strengths. For example, the relative XPS intensities for the transitions involving the SO-split states are approximated as

$$\tilde{\boldsymbol{\gamma}}^2 = \mathbf{U}^\dagger \boldsymbol{\gamma}^L \boldsymbol{\gamma}^R \mathbf{U}. \tag{21}$$

The SOC-CVS-EOM-CCSD approach has been implemented in the Q-Chem electronic structure package.[64,65] The implementation included the extension of the fc-CVS-EOM-CCSD framework to the SF states, in addition to the previously implemented[23,24] IP and

EE variants. For the XPS calculations, we used the 6-311+G(3*df*) basis set with uncontracted core functions, denoted as uC-6-311+G(3*df*), following the recommendation of a recent benchmark study.[6] Because we focus on L-edges, we only uncontracted the core orbitals roughly corresponding to $n = 2$, i.e., second contracted s-function (leaving the '6' contracted core function untouched) and the two most contracted p-functions. For the XAS calculations, we used uC-6-311(2+,+)G(p, d) augmented with additional Rydberg-type functions whose exponents were generated according to the prescription of Kaufmann et al.,[66] and quantum number $n = 2.5, \ldots, 5$. Uncontracted bases were used for the active edge only, whereas all other atoms were described by the standard variants of these basis sets. All basis sets are given in the SI.

The number of states included in the SOMF Hamiltonian varies depending on the system, the exact number of states for each system can be found in SI.

To illustrate the capabilities of the method, we considered several systems for which experimental data are available. These systems are listed in Table S1, along with their structural parameters. In most cases, we used structures optimized at the CCSD(T)/cc-pCVQZ level of theory, taken from Ref. 67. For thiophene, we used an MP2/cc-pVTZ optimized structure. All Cartesian coordinates are given in the SI.

Table 1 shows the first three core-ionization energies (IEs) in eV for H_2S, OCS, SO_2, CS_2, and $C_4H_4S_2$ computed with SOC-CVS-EOMIP-CCSD/uC-6-311+G(3*df*).

Table 1: L-edge ionization energies (eV) and SO splitting (cm^{-1}) obtained at the fc-CVS-EOMIP-CCSD level of theory using the uC-6-311+G(3*df*) basis set.

System	Ass.	IE (eV)	ΔE (cm^{-1})
$H_2\mathbf{S}$	$2p_{3/2}^{-1}$	169.405	0.00
		169.495	726.54
	$2p_{1/2}^{-1}$	170.648	10025.40
OC**S**	$2p_{3/2}^{-1}$	169.996	0.00
		170.108	901.43
	$2p_{1/2}^{-1}$	171.254	10145.25
$\mathbf{S}O_2$	$2p_{3/2}^{-1}$	174.341	0.00
		174.410	559.04
	$2p_{1/2}^{-1}$	175.575	9949.94
$C\mathbf{S}_2$	$2p_{3/2}^{-1}$	169.618	0.00
		169.618	0.06
		169.708	724.46
		169.708	727.00
	$2p_{1/2}^{-1}$	170.860	10018.78
		170.860	10020.21
$C_4H_4\mathbf{S}$	$2p_{3/2}^{-1}$	169.390	0.00
		169.458	546.15
	$2p_{1/2}^{-1}$	170.620	9913.76

These are tabulated together with the energy difference with respect to the first IE (ΔE) in cm^{-1}. The corresponding zeroth-order energies, calculated at the non-relativistic fc-CVS-EOMIP-CCSD/uC-6-311+G(3*df*) level of theory are given in Table S2. The energies are assigned to the ionization of the electrons from the $2p$ orbitals of the atom marked in bold. The results show how spin-orbit coupling splits the nearly degenerate $2p$ orbitals into two sets: one $2p_{1/2}$ orbital and two near-degenerate $2p_{3/2}$ orbitals, as explained in Fig. 1 and illustrated in Fig. 2. The gap between these two sets is due to the spin-orbit effects, whereas the small energy difference between the $2p_{3/2}$ orbitals arises from non-spherically symmetric molecular environment; this latter splitting is called molecular field splitting. Fig. 3 shows the computed XPS spectra of the thiophene molecule, illustrating the spectroscopic signatures of the SOC. At the non-relativistic level, the $2p$ orbitals, although already slightly non-degenerate due to the molecular field, are still close enough so that the spectrum has only one

peak. The inclusion of SOC splits this peak into two, with intensity ratio 2:1, corresponding to the ionization of two $2p_{3/2}$ and the one $2p_{1/2}$. After a shift of +0.5 eV the SO-corrected spectrum agrees well with the experiment, both in terms of the the intensity ratio and the energy splitting.

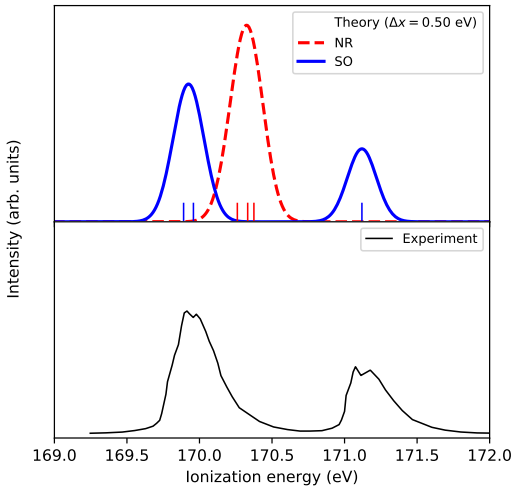

Figure 3: Thiophene (C_4H_4S) L-edge XPS theoretical and experimental spectra. The theoretical spectra were obtained using a Gaussian convolution function ($\sigma = 0.15$ eV) and an energy shift of +0.5 eV, estimated by aligning to the first intense experimental peaks. The experimental spectrum was digitized from Ref. 68.

Fig. 4 compares the computed NEXAFS L-edge spectra for SiH_4, SO_2, C_4H_4S, and Ar with the experimental spectra. The raw theoretical data (energies and oscillator strengths) can be found in SI.

Fig. 4a shows the L-edge spectra of silane with and without SOCs. The first peak is split into two upon inclusion of SOC, as in the XPS example above, and agrees well with the experiment.

The shifted IEs are also well reproduced. However, our convoluted spectrum do not reproduce the highly structured set of bands above 104.4 eV observed in the experiment, possibly due to using the same empirical Gaussian broadening function for all computed states, regardless of their actual lifetime.

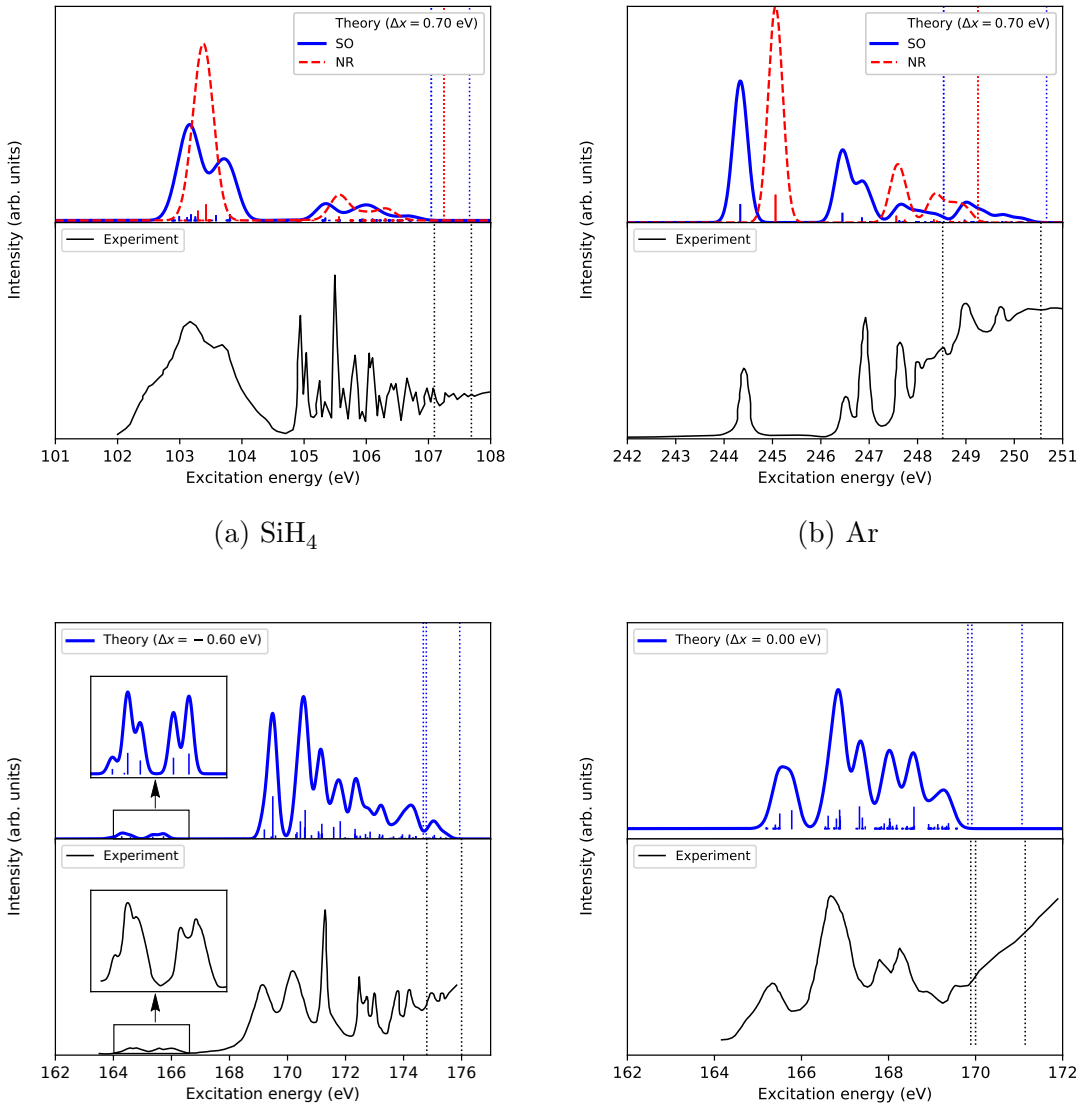

(a) SiH_4 (b) Ar

(c) SO_2 (d) Thiophene, C_4H_4S

Figure 4: L-edge XAS theoretical and experimental spectra of: SiH_4 (4a), Ar (4b), SO_2 (4c) and C_4H_4S (4d). The theoretical spectra were obtained using a Gaussian convolution function ($\sigma = 0.15$ eV) and an energy shift (Δx) for a better fit with experiment. The experimental spectra were digitized from Ref. 69 for SiH_4, Ref. 70 for Ar, Ref. 71 for SO_2 and Ref. 72 for thiophene. The vertical dotted lines correspond to the L_2 and L_3 ionization energies. The label NR denotes non-relativistic calculations without inclusion of the SOC.

Fig. 4b shows the spectra for the argon atom. Theory and experiment agree well, after a small shift of only +0.7 eV. The first band at around 244.5 eV is due to the $2p_{3/2} \rightarrow 4s$ transition, whereas the second band at around 246.5 eV corresponds to the $2p_{1/2} \rightarrow 4s$

transition. The third and forth bands contain contributions from the $2p_{3/2} \rightarrow \ 5s, 3d$ and $2p_{1/2} \rightarrow \ 5s, 3d$ transitions, respectively. In the case of sulfur dioxide, see Fig. 4c, the agreement between theory and experiment is also quite good for the first peaks (zoomed-in region), after a shift of -0.6 eV is applied. The agreement slightly deteriorates at higher energies.

Finally, Fig. 4d illustrates the spectra for the slightly larger molecule, thiophene. In this case, the theoretical spectrum is in excellent agreement with the experimental one in the entire energy range and without energy shift.

In conclusion, we have presented the first implementation of the perturbative inclusion of spin-orbit effects within coupled-cluster theory to describe the spectroscopy of core states. This has been achieved by applying a general framework for calculating the SOCs using spinless one-particle density matrices corresponding to the fc-CVS-EOM-CCSD states. This methodological advance enables the calculation of SO-corrected ionization and excitation energies by a simple two-step procedure. In the first step, the non-relativistic states are computed using appropriate variants of the EOM-CC family of methods, depending on the target states (IP for ionized states and EE/SF for excited states). In the second step, these zeroth-order states are mixed by the perturbation due to the SO part of the Breit-Pauli Hamiltonian, giving rise to the SO-corrected energies and intensities. The examples illustrate the capabilities of the new method to accurately and efficiently simulate L-edge XAS and XPS spectra.

Acknowledgement

S.C. thanks Professor Lan Cheng from the Johns Hopkins University for valuable discussions during the initial phase of this project. M.L.V. and S.C. acknowledge financial support from DTU Chemistry (Ph.D. grant to M.L.V) and from the Independent Research Fund Denmark—Natural Sciences (Research-Project-2 grant No. 7014-00258B to S.C.). The work

at USC was supported by the U.S. National Science Foundation (No. CHE-1856342 to A.I.K.).

Note

The authors declare the following competing financial interest(s): A. I. K. is the President and a part-owner of Q-Chem, Inc.

Supporting Information Available

Additional information: Cartesian coordinates, basis sets, zeroth-order IEs and spectroscopic data (raw data for XAS of Ar, H_2S, OCS, SO_2 SiH_4 and C_4H_4S, and XAS spectra of OCS and H_2S).

References

(1) van Bokhoven, J. A., Lamberti, C., Eds. *X-Ray Absorption and X-ray Emission Spectroscopy; Theory and Applications*; Wiley & Sons, 2016.

(2) Mobilio, S., Boscherini, F., Meneghini, C., Eds. *Synchrotron Radiation: Basics, Methods and Applications*; Springer, 2014.

(3) Bergmann, U., Yachandra, V. K., Yano, J., Eds. *X-Ray Free Electron Lasers: Applications in Materials, Chemistry and Biology*; Energy and Environment Series 18; Royal Society of Chemistry, 2017.

(4) Norman, P.; Dreuw, A. Simulating X-ray Spectroscopies and Calculating Core-Excited States of Molecules. *Chem. Rev.* **2018**, *118*, 7208–7248.

(5) Carbone, J. P.; Cheng, L.; Myhre, R. H.; Matthews, D.; Koch, H.; Coriani, S. Chapter Eleven - An analysis of the performance of coupled cluster methods for K-edge core

excitations and ionizations using standard basis sets. In *State of The Art of Molecular Electronic Structure Computations: Correlation Methods, Basis Sets and More*; Ancarani, L. U., Hoggan, P. E., Eds.; Adv. Quantum Chem.; Academic Press, 2019; Vol. 79; pp 241 – 261.

(6) Sarangi, R.; Vidal, M. L.; Coriani, S.; Krylov, A. I. On the basis set selection for calculations of core-level states: different strategies to balance cost and accuracy. *Mol. Phys.* **2020**, *0*, e1769872.

(7) Sekino, H.; Bartlett, R. J. A linear response, coupled-cluster theory for excitation energy. *Int. J. Quant. Chem.* **1984**, *26*, 255–265.

(8) Stanton, J. F.; Bartlett, R. J. The equation of motion coupled-cluster method. A systematic biorthogonal approach to molecular excitation energies, transition probabilities, and excited state properties. *J. Chem. Phys.* **1993**, *98*, 7029–7039.

(9) Krylov, A. I. Equation-of-Motion Coupled-Cluster Methods for Open-Shell and Electronically Excited Species: The Hitchhiker's Guide to Fock Space. *Ann. Rev. Phys. Chem.* **2008**, *59*, 433–462.

(10) Bartlett, R. J. Coupled-cluster theory and its equation-of-motion extensions. *WIREs Comput Mol Sci* **2012**, *2*, 126–138.

(11) Sneskov, K.; Christiansen, O. Excited state coupled cluster methods. *WIREs Comput. Mol. Sci.* **2012**, *2*, 566–584.

(12) Coriani, S.; Pawłowski, F.; Olsen, J.; Jørgensen, P. Molecular response properties in equation of motion coupled cluster theory: A time-dependent perspective. *J. Chem. Phys.* **2016**, *144*, 024102.

(13) Sadybekov, A.; Krylov, A. I. Coupled-cluster based approach for core-ionized and core-

excited states in condensed phase: Theory and application to different protonated forms of aqueous glycine. *J. Chem. Phys.* **2017**, *147*, 014107.

(14) Faber, R.; Coriani, S. Corevalence-separated coupled-cluster-singles-and-doubles complex-polarization-propagator approach to X-ray spectroscopies. *Phys. Chem. Chem. Phys.* **2020**, *22*, 2642.

(15) Cederbaum, L. S.; Domcke, W.; Schirmer, J. Many-body theory of core holes. *Phys. Rev. A: At. Mol. Opt. Phys.* **1980**, *22*, 206–222.

(16) Barth, A.; Schirmer, J. Theoretical core-level excitation spectra of N_2 and CO by a new polarisation propagator method. *J. Phys. B: At. Mol. Phys.* **1985**, *18*, 867–885.

(17) Trofimov, A. B.; Moskovskaya, T. E.; Gromov, N. M., E. V. Vitkovskaya; Schirmer, J. Core-level electronic spectra in ADC(2) approximation for polarization propagator: carbon monoxide and nitrogen molecules. *J. Struct. Chem.* **2000**, *41*, 483–494.

(18) Stener, M.; Fronzoni, G.; de Simone, M. Time Dependent Density Functional Theory of Core Electrons Excitations. *Chem. Phys. Lett.* **2003**, *15*, 115.

(19) Wenzel, J.; Wormit, M.; Dreuw, A. Calculating Core-Level Excitations and X-Ray Absorption Spectra of Medium-Sized Closed-Shell Molecules with the Algebraic-Diagrammatic Construction Scheme for the Polarization Propagator. *J. Comput. Chem.* **2014**, *35*, 1900.

(20) Wenzel, J.; Holzer, A.; Wormit, M.; Dreuw, A. Analysis and Comparison of CVS-ADC Approaches up to Third Order for the Calculation of Core-Excited States. *J. Chem. Phys.* **2015**, *142*, 214104.

(21) Delcey, M. G.; Srensen, L. K.; Vacher, M.; Couto, R. C.; Lundberg, M. Efficient calculations of a large number of highly excited states for multiconfigurational wavefunctions. *J. Comput. Chem.* **2019**, *40*, 1789–1799.

(22) Coriani, S.; Koch, H. Communication: X-ray Absorption Spectra and Core-Ionization Potentials within a Core-Valence Separated Coupled Cluster Framework. *J. Chem. Phys.* **2015**, *143*, 181103.

(23) Vidal, M. L.; Feng, X.; Epifanovsky, E.; Krylov, A. I.; Coriani, S. New and Efficient Equation-of-Motion Coupled-Cluster Framework for Core-Excited and Core-Ionized States. *J. Chem. Theory Comput.* **2019**, *15*, 3117–3133.

(24) Vidal, M. L.; Krylov, A. I.; Coriani, S. Dyson orbitals within the fc-CVS-EOM-CCSD framework: theory and application to X-ray photoelectron spectroscopy of ground and excited states. *Phys. Chem. Chem. Phys.* **2020**, *22*, 2693.

(25) Frati, F.; De Groot, F.; Cerezo, J.; Santoro, F.; Cheng, L.; Faber, R.; Coriani, S. Coupled cluster study of the x-ray absorption spectra of formaldehyde derivatives at the oxygen, carbon, and fluorine K-edges. *J. Chem. Phys.* **2019**, *151*, 064107.

(26) Myhre, R. H.; Coriani, S.; Koch, H. Near-edge X-ray absorption fine structure within multilevel coupled cluster theory. *J. Chem. Theory Comput.* **2016**, *12*, 2633–2643.

(27) Liu, J.; Matthews, D.; Coriani, S.; Cheng, L. Benchmark Calculations of K-Edge Ionization Energies for First-Row Elements Using Scalar-Relativistic Core–Valence-Separated Equation-of-Motion Coupled-Cluster Methods. *J. Chem. Theory Comput.* **2019**, *15*, 1642–1651.

(28) Tenorio, B. N. C.; Moitra, T.; Nascimento, M. A. C.; Rocha, A. B.; Coriani, S. Molecular inner-shell photoabsorption/photoionization cross sections at core-valence-separated coupled cluster level: Theory and examples. *J. Chem. Phys.* **2019**, *150*, 224104.

(29) Faber, R.; Coriani, S. Resonant Inelastic X-ray Scattering and Nonesonant X-ray Emission Spectra from Coupled-Cluster (Damped) Response Theory. *J. Chem. Theory Comput.* **2019**, *15*, 520–528.

(30) Nanda, K.; Vidal, M. L.; Faber, R.; Coriani, S.; Krylov, A. I. How to stay out of trouble in RIXS calculations within the equation-of-motion coupled-cluster damped response theory framework? Safe hitchhiking in the excitation manifold by means of core-valence separation. *Phys. Chem. Chem. Phys.* **2020**, *22*, 2629.

(31) Nanda, K.; Krylov, A. I. A simple molecular orbital picture of RIXS distilled from many-body damped response theory. *J. Chem. Phys.* **2020**, in press.

(32) Pyykko, P. Relativistic effects in structural chemistry. *Chem. Rev.* **1988**, *88*, 563–594.

(33) Coriani, S.; Christiansen, O.; Fransson, T.; Norman, P. Coupled-Cluster Response Theory for Near-Edge X-Ray-Absorption Fine Structure of Atoms and Molecules. *Phys. Rev. A* **2012**, *85*, 022507.

(34) Saue, T. Relativistic Hamiltonians for chemistry: A primer. *ChemPhysChem* **2011**, *12*, 3077–3094.

(35) Visscher, L.; Lee, T. J.; Dyall, K. G. Formulation and implementation of a relativistic unrestricted coupled-cluster method including noniterative connected triples. *J. Chem. Phys.* **1996**, *105*, 8769–8776.

(36) Shee, A.; Visscher, L.; Saue, T. Analytic one-electron properties at the 4-component relativistic coupled cluster level with inclusion of spin-orbit coupling. *J. Chem. Phys.* **2016**, *145*, 184107.

(37) Shee, A.; Saue, T.; Visscher, L.; Gomes, A. S. P. Equation-of-motion coupled-cluster theory based on the 4-component Dirac-Coulomb(-Gaunt) Hamiltonian. Energies for single electron detachment, attachment, and electronically excited states. *J. Chem. Phys.* **2018**, *149*, 174113.

(38) Chang, C.; Pelissier, M.; Durand, P. Regular two-component Pauli-like effective Hamiltonians in Dirac theory. *Physica Scripta* **1986**, *34*, 394.

(39) Lenthe, E. v.; Baerends, E.-J.; Snijders, J. G. Relativistic regular two-component Hamiltonians. *J. Chem. Phys.* **1993**, *99*, 4597–4610.

(40) van Lenthe, E.; Baerends, E.-J.; Snijders, J. G. Relativistic total energy using regular approximations. *J. Chem. Phys.* **1994**, *101*, 9783–9792.

(41) Van Lenthe, E.; Snijders, J. G.; Baerends, E. J. The zero-order regular approximation for relativistic effects: The effect of spin–orbit coupling in closed shell molecules. *J. Chem. Phys.* **1996**, *105*, 6505–6516.

(42) Dyall, K. G.; van Lenthe, E. Relativistic regular approximations revisited: An infinite-order relativistic approximation. *J. Chem. Phys.* **1999**, *111*, 1366–1372.

(43) Douglas, M.; Kroll, N. M. Quantum electrodynamical corrections to the fine structure of helium. *Annals of Physics* **1974**, *82*, 89–155.

(44) Hess, B. A. Relativistic electronic-structure calculations employing a two-component no-pair formalism with external-field projection operators. *Phys. Rev. A* **1986**, *33*, 3742.

(45) Jansen, G.; Heß, B. A. Revision of the Douglas-Kroll transformation. *Phys. Rev. A* **1989**, *39*, 6016.

(46) Iliaš, M.; Saue, T. An infinite-order two-component relativistic Hamiltonian by a simple one-step transformation. *J. Chem. Phys.* **2007**, *126*, 064102.

(47) Filatov, M.; Zou, W.; Cremer, D. Spin-orbit coupling calculations with the two-component normalized elimination of the small component method. *J. Chem. Phys.* **2013**, *139*, 014106.

(48) Cheng, L.; Wang, F.; Stanton, J. F.; Gauss, J. Perturbative treatment of spin-orbit-coupling within spin-free exact two-component theory using equation-of-motion coupled-cluster methods. *J. Chem. Phys.* **2018**, *148*, 044108.

(49) Fleig, T. Time-reversal symmetry in general coupled cluster theory. *Phys. Rev. A* **2008**, *77*, 062503.

(50) Wahlgren, U.; Sjøvoll, M.; Fagerli, H.; Gropen, O.; Schimmelpfennig, B. Ab initio calculations of the $^2P_{1/2} - {}^2P_{3/2}$ splitting in the thallium atom. *Theor. Chem. Acc.* **1997**, *97*, 324–330.

(51) Christiansen, O.; Gauss, J.; Schimmelpfennig, B. Spin-orbit coupling constants from coupled-cluster response theory. *Phys. Chem. Chem. Phys.* **2000**, *2*, 965–971.

(52) Klein, K.; Gauss, J. Perturbative calculation of spin-orbit splittings using the equation-of-motion ionization-potential coupled-cluster ansatz. *J. Chem. Phys.* **2008**, *129*, 194106.

(53) Mück, L. A.; Gauss, J. Communication: Spin-orbit splittings in degenerate open-shell states via Mukherjee's multireference coupled-cluster theory: A measure for the coupling contribution. *J. Chem. Phys.* **2012**, *136*, 111103.

(54) Epifanovsky, E.; Klein, K.; Stopkowicz, S.; Gauss, J.; Krylov, A. I. Spin-orbit couplings within the equation-of-motion coupled-cluster framework: Theory, implementation, and benchmark calculations. *J. Chem. Phys.* **2015**, *143*, 064102.

(55) Pokhilko, P.; Epifanovsky, E.; Krylov, A. I. General framework for calculating spinorbit couplings using spinless one-particle density matrices: Theory and application to the equation-of-motion coupled-cluster wave functions. *J. Chem. Phys.* **2019**, *151*, 034106.

(56) Pokhilko, P.; Krylov, A. I. Quantitative El-Sayed Rules for Many-Body Wavefunctions from Spinless Transition Density Matrices. *J. Phys. Chem. Lett.* **2019**, *10*, 4857–4862.

(57) Reiher, M.; Wolf, A. *Relativistic quantum chemistry: the fundamental theory of molecular science*; John Wiley & Sons, 2014.

(58) Helgaker, T.; Coriani, S.; Jørgensen, P.; Kristensen, K.; Olsen, J.; Ruud, K. Recent Advances in Wave Function-Based Methods of Molecular-Property Calculations. *Chem. Rev.* **2012**, *112*, 543–631.

(59) Hess, B. A.; Marian, C. M.; Wahlgren, U.; Gropen, O. A mean-field spin-orbit method applicable to correlated wavefunctions. *Chem. Phys. Lett.* **1996**, *251*, 365–371.

(60) Oana, C. M.; Krylov, A. I. Dyson orbitals for ionization from the ground and electronically excited states within equation-of-motion coupled-cluster formalism: Theory, implementation, and examples. *J. Chem. Phys.* **2007**, *127*, 234106.

(61) Oana, C. M.; Krylov, A. I. Cross sections and photoelectron angular distributions in photodetachment from negative ions using equation-of-motion coupled-cluster Dyson orbitals. *J. Chem. Phys.* **2009**, *131*, 124114.

(62) Moitra, T.; Ponzi, A.; Koch, H.; Coriani, S.; Decleva, P. Accurate Description of Photoionization Dynamical Parameters. *J. Phys. Chem. Lett.* **2020**, *11*, 5330–5337.

(63) Mai, S.; Plasser, F.; Dorn, J.; Fumanal, M.; Daniel, C.; González, L. Quantitative wave function analysis for excited states of transition metal complexes. *Coord. Chem. Rev.* **2018**, *361*, 74–97.

(64) Krylov, A. I.; Gill, P. M. W. Q-Chem: An engine for innovation. *WIREs Comput. Mol. Sci.* **2013**, *3*, 317–326.

(65) Shao, Y.; Gan, Z.; Epifanovsky, E.; Gilbert, A. T.; Wormit, M.; Kussmann, J.; Lange, A. W.; Behn, A.; Deng, J.; Feng, X. et al. Advances in molecular quantum chemistry contained in the Q-Chem 4 program package. *Mol. Phys.* **2015**, *113*, 184–215.

(66) Kaufmann, K.; Baumeister, W.; Jungen, M. Universal Gaussian basis sets for an opti-

mum representation of Rydberg and continuum wavefunctions. *J. Phys. B: At., Mol. Opt. Phys.* **1989**, *22*, 2223.

(67) Coriani, S.; Marchesan, D.; Gauss, J.; Hättig, C.; Helgaker, T.; Jørgensen, P. The accuracy of ab initio molecular geometries for systems containing second-row atoms. *J. Chem. Phys.* **2005**, *123*, 184107.

(68) Siggel, M. R. F.; Field, C.; Sæthre, L. J.; Børve, K. J.; Thomas, T. D. High resolution photoelectron spectroscopy of sulfur 2p electrons in H_2S, SO_2, CS_2, and OCS. *J. Chem. Phys.* **1996**, *105*, 9035–9039.

(69) Püttner, R.; Domke, M.; Lentz, D.; Kaindl, G. Si $2p$ photoabsorption in SiH_4 and SiD_4: Molecular distortion in core-excited silane. *Phys. Rev. A* **1997**, *56*, 1228–1239.

(70) Nakamura, M.; Sasanuma, M.; Sato, S.; Watanabe, M.; Yamashita, H.; Iguchi, Y.; Ejiri, A.; Nakai, S.; Yamaguchi, S.; Sagawa, T. et al. Absorption Structure Near the $L_{II,III}$ Edge of Argon Gas. *Phys. Rev. Lett.* **1968**, *21*, 1303.

(71) Krasnoperova, A. A.; Gluskin, E. S.; Mazalov, L. N.; Kochubei, V. A. The fine structure of the $L_{II,III}$ absorption edge of sulfur in the SO_2 molecule. *J. Struct. Chem.* **1976**, *17*, 947–950.

(72) Baseggio, O.; Toffoli, D.; Stener, M.; Fronzoni, G.; de Simone, M.; Grazioli, C.; Coreno, M.; Guarnaccio, A.; Santagata, A.; DAuria, M. S2p core level spectroscopy of short chain oligothiophenes. *J. Chem. Phys.* **2017**, *147*, 244301.